https://doi.org/10.5194/egusphere-2023-1155
Preprint. Discussion started: 6 July 2023

Sensitivity of atmospheric rivers to aerosol treatment in regional climate simulations: Insights from the AIRA identification algorithm

Eloisa Raluy-López[1], Juan Pedro Montávez[1], and Pedro Jiménez-Guerrero[1,2]

[1]Physics of the Earth, Regional Campus of International Excellence (CEIR) "Campus Mare Nostrum", University of Murcia, Spain.
[2]Biomedical Research Institute of Murcia (IMIB-Arrixaca), Spain.

Correspondence: Juan P. Montávez (montavez@um.es); Pedro Jiménez-Guerrero (pedro.jimenezguerrero@um.es)

Abstract. This study analyzed the sensitivity of Atmospheric Rivers (ARs) to aerosol treatment in regional climate simulations. Three experiments covering the Iberian Peninsula for the period 1991 to 2010 were examined, each including prescribed aerosols (BASE), direct and semi-direct aerosol effects (ARI), and direct, semi-direct, and indirect aerosol effects (ARCI). A new regional-scale AR identification algorithm, AIRA, was developed and used to identify around 250 ARs in each experiment. The results showed that spring and autumn ARs were the most frequent, intense, and long-lasting, and that ARs could explain up to a 30% of the total accumulated precipitation. The inclusion of aerosols was found to redistribute precipitation, with increases in the areas of AR occurrence. The analysis of common AR events showed that the differences between simulations were minimal in the most intense cases, and a negative correlation was found between mean direction and mean latitude differences. The joint analysis and classification of dust and sea salt aerosol distributions allowed clustering of common events into eight main aerosol configurations in ARI and ARCI. The sensitivity of ARs to different aerosol treatments was observed to induce spatial deviations and intensity reinforcements/attenuations depending on the aerosol configuration. The correct inclusion of aerosol effects is thus important for the simulation of AR behavior at both global and regional scales, which is essential for meteorological predictions and climate change projections.

1 Introduction

Atmospheric rivers (ARs) are long and narrow structures with high water vapor concentration that transport up to 90% of moisture from the tropics to mid-latitudes and the poles (Gimeno et al., 2014; Zhu and Newell, 1998). ARs provide a significant source of water in the form of rain or snow, enabling the regeneration of water resources in areas where they make landfall. However, they are also associated with extreme precipitation events (Trigo et al., 2015; Eiras-Barca et al., 2018). ARs are typically situated in the warm conveyor belts of extratropical cyclones and are associated with strong winds at low levels. At any given time, there are usually 4-5 ARs on a global scale (Zhu and Newell, 1998), since each planetary wave is generally linked to an extratropical cyclone on a synoptic scale (Ralph et al., 2004). The number of ARs increases during autumn and winter months, as extratropical cyclones are more frequent during these seasons (Gimeno et al., 2014).

With the advent of weather satellites and atmospheric general circulation models, research on ARs has considerably increased. From the beginning, the West Coast of the United States (Lorente-Plazas et al., 2018; Guan et al., 2012) and the

https://doi.org/10.5194/egusphere-2023-1155
Preprint. Discussion started: 6 July 2023

Pacific Ocean (Ralph et al., 2004, 2011) have been the most studied regions. However, a multitude of different studies have been carried out more recently trying to shed light on ARs all around the world. The modification of ARs due to climate change is currently of great research interest. Some authors suggest that an increased atmospheric moisture due to global warming will lead to an intensification of ARs activity and to a potential enhancement of the AR-related precipitation (Payne et al., 2020; Algarra et al., 2020). Another topic of great interest is the influence of ARs on the Arctic Sea ice, as they have been related with a slowing of the ice seasonal recovery (Zhang et al., 2023). Western Europe has been the focus of several studies in the last decade. These studies have demonstrated a connection between ARs and their Mediterranean variant (Lorente-Plazas et al., 2020) with some of the heaviest rainfall recorded in the Iberian Peninsula (IP) (Trigo et al., 2015; Eiras-Barca et al., 2018). In addition, up to 90% of anomalous rainfall in some IP areas coincides with the arrival of ARs. This percentage has a maximum in winter and a minimum in mid-spring (Eiras-Barca et al., 2018). A more recent study has characterized the strength and impacts of ARs on the European west coast by adapting and applying the AR Scale (Ralph et al., 2019) to Europe (Eiras-Barca et al., 2021).

The importance of ARs has given rise to numerous identification algorithms with a wide range of methodologies. This diversity is, among others, due to the ongoing need of establishing a robust AR definition (Gimeno et al., 2021). The Third ARTMIP Workshop (O'Brien et al., 2020) contemplates the existence of different "flavors" of ARs, although most tracking methods have not considered this possibility yet. This report also states the need of creating a common software infrastructure and classifying AR algorithms to understand the broad uncertainty in AR detection results. An IVT magnitude greater than 250 kg m^{-1} s^{-1} and a length over 2,000 km would be considered an AR according to some algorithms (Zhu and Newell, 1998) but not to others. Percentiles of the IVT or IWV fields, typically the 85^{th} or 90^{th} percentile, have also been utilized (Lavers et al., 2012). Future AR researches would also be able to apply machine-learning techniques easily (O'Brien et al., 2020). These algorithms are mainly applied to the outputs of global climate models (GCMs) and reanalysis (Gimeno et al., 2014). Therefore, most of them consist of detecting the arrival of the potential AR and spatially tracking its long 2D structure until it is delimited for that fixed time. However, inaccuracies in the forecasted precipitation intensity, frequency and spatial variability due to the arrival of an AR on a local scale are encountered. As ARs interact with orography on a regional scale, GCMs can represent ARs but may not accurately reproduce their behavior (Lorente-Plazas et al., 2018). In such cases, the use of regional climate models (RCMs) with higher resolution can provide a better understanding of ARs. This is the case of the IP, characterised by a complex orography. Nevertheless, it should be taken into account that the spatial tracking given a fixed time step method is not suitable for data obtained from RCMs, as the spatial domain is limited.

Several researchers have investigated the role of atmospheric rivers (ARs) and similar structures in the global transport of atmospheric aerosols (Chakraborty et al., 2021). However, the impact of these aerosols and their variability on the formation, characteristics, and behavior of ARs has received less attention. RCMs typically introduce aerosol species and their concentrations in a prescribed manner (Forkel et al., 2015), neglecting changes in their concentration and interactions with radiation and cloud microphysics. In contrast, a coupled online approach for aerosol calculation allows the effects of aerosols on radiation and clouds (i.e., direct, semi-direct, and indirect effects) to be quantified from a climate perspective (López-Romero et al., 2021). This approach can lead to variations between simulated meteorological situations and those obtained by using a

https://doi.org/10.5194/egusphere-2023-1155
Preprint. Discussion started: 6 July 2023

prescribed aerosol configuration, potentially resulting in changes in the frequency, intensity, or landfall areas of ARs and their consequences across all sectors, both environmental and socio-economic.

The primary objective of this study is to evaluate the influence of atmospheric aerosols and their interactions with solar radiation and cloud microphysics processes on ARs that impact the IP region. To achieve this goal, a comparative analysis of regional climate simulations with different levels of interactions between aerosols, radiation, and cloud microphysics is required.

This study employs an AR identification algorithm that processes data from regional-scale simulations to verify its accuracy for the IP region. The developed identification algorithm is then applied to three experiments: BASE, ARI, and ARCI. The BASE simulation uses a prescribed aerosol configuration and serves as the reference. The ARI simulation includes dynamic aerosol-radiation interactions (i.e., direct and semi-direct effects). Finally, the ARCI experiment includes aerosol interactions with both radiation and cloud microphysics, accounting for direct, semi-direct, and indirect effects. By comparing the results of these experiments, we can evaluate the impact of atmospheric aerosols and their interactions on ARs affecting the IP region.

2 Methods

2.1 Data

The data used in this study were derived from the REPAIR project, which involved regional climate simulations for Europe spanning the period 1991-2010 at hourly resolution. The WRF-Chem model (v.3.6.1) was used for the simulations, both in a decoupled configuration (WRF alone (Skamarock et al., 2008)) and in a fully coupled configuration with atmospheric chemistry and pollutant transport to account for aerosol-radiation and aerosol-cloud interactions (Grell et al., 2005). The initial and boundary conditions were obtained from the ERA20-C reanalysis (López-Romero et al., 2021).

The spatial configuration included two one-way nested domains, with the inner domain covering Europe with a resolution of 0.44° in latitude and longitude following the Euro-CORDEX recommendations (Jacob et al., 2014). The outer domain had a spatial resolution of about 150 km and extended southwards to a latitude of 20°N to encompass major dust emission areas, which were incorporated into the inner domain via boundary conditions (Palacios-Peña et al., 2019). The vertical domain comprised 29 non-uniform sigma levels with higher resolution near the surface, subsequently interpolated to pressure levels. The upper boundary was set at the 50 hPa level.

Three experiments were considered in this study, each of which included different aerosol interactions (Jerez et al., 2021). The BASE experiment served as a reference, with aerosols not treated interactively in the model, but prescribed with an aerosol optical depth (AOD) set to zero and 250 CCN/cm^3 considered in each domain cell. This experiment did not account for the effects of aerosols on radiation and cloud microphysics. In the ARI experiment, aerosols were treated online, and the aerosol-radiation interactions were activated in the model (Fast et al., 2006). The CCN concentration was the same as that in the BASE experiment. Thus, this simulation only accounted for the direct and semi-direct effects of aerosols. In the ARCI experiment, aerosol interactions with cloud microphysics (indirect effects) were also activated.

https://doi.org/10.5194/egusphere-2023-1155
Preprint. Discussion started: 6 July 2023

In the ARI and ARCI experiments, aerosols were calculated in the WRF-Chem model using a coupled approach, where the model solved the aerosol dynamics online, allowing it to incorporate its own aerosols based on variables such as soil type, vegetation, and wind at each point of the domain (López-Romero et al., 2021). The simulations included five aerosol species: sulphates, mineral dust, sea salt, organic matter, and black carbon. The WRF-Chem model's aerosol-radiation-cloud interactions were explained in detail by Palacios-Peña et al. (2018). To calculate aerosol-radiation interactions, each species was associated with a complex refractive index. Mie's theory was used to obtain the optical properties of the aerosols in each cell by summing up the contributions from all aerosol sizes and species, which were then incorporated into the solar radiation scheme. The ARCI experiment's description and aerosol validation results were reported in Palacios-Peña et al. (2020). Aerosol-cloud interactions were included by connecting the number of simulated cloud droplets to the Goddard solar radiation scheme, representing the first indirect effect, and to Lin's microphysics parameterisation (Lin et al., 1983), representing the second indirect effect. Consequently, the number of droplets affected both their mean radius and the optical depth of the cloud. The WRF-Chem model facilitated converting the single-momentum Lin parameterisation into a double-momentum one. Additional information on the physical setup of the experiments (i.e., the land surface model, radiative scheme, or atmospheric boundary layer parameterisation) is available in Jerez et al. (2021).

2.2 The AR identification algorithm: AIRA

The identification of ARs on a global scale does not apply to regional climate simulations due to the limited spatial domain. Consequently, it is impossible to determine the complete length of an AR by tracking its structure for a fixed duration. To address this issue, a new AR identification algorithm, named AIRA, has been developed. AIRA is designed to work with regional data and utilizes Integrated water Vapor Transport (IVT) as its basis. IVT is a horizontal vector that is defined by Equations 1 and 2, where q represents the specific humidity, u and v refer to the zonal and meridional wind components and $g_0 = 9.81$ m s^{-2} is the gravity acceleration at sea level.

$$IVT_u = \frac{1}{g_0} \int_{1000\ hPa}^{300\ hPa} qu\ dP \tag{1}$$

$$IVT_v = \frac{1}{g_0} \int_{1000\ hPa}^{300\ hPa} qv\ dP \tag{2}$$

Equations 1 and 2 can be numerically solved by calculating the sum of the product of specific humidity and wind component values at a given pressure level, and the pressure increment between that level and the level below it (Equation 3). The magnitude and direction of the IVT with respect to the East can then be easily obtained. The magnitude of the IVT is expressed in kg m^{-1} s^{-1}, while its direction is calculated in degrees East and is positive in the counter-clockwise direction. AIRA primarily utilizes the magnitude and direction of the IVT in its functioning.

https://doi.org/10.5194/egusphere-2023-1155
Preprint. Discussion started: 6 July 2023

$$IVT_u = \frac{1}{g_0}\sum_i q_i\, u_i\, \Delta P_i, \quad IVT_v = \frac{1}{g_0}\sum_i q_i\, v_i\, \Delta P_i \tag{3}$$

AIRA relies on two fixed longitude detection lines to identify atmospheric rivers. The main detection line, referred to as line 1 (L1), is located closest to the region of interest and is used to analyze the magnitude of the IVT. The second line (L2) serves as an auxiliary line to study the direction of potential AR candidates that pass through L2 before reaching L1. Figure 1 illustrates the detection lines utilized in this study.

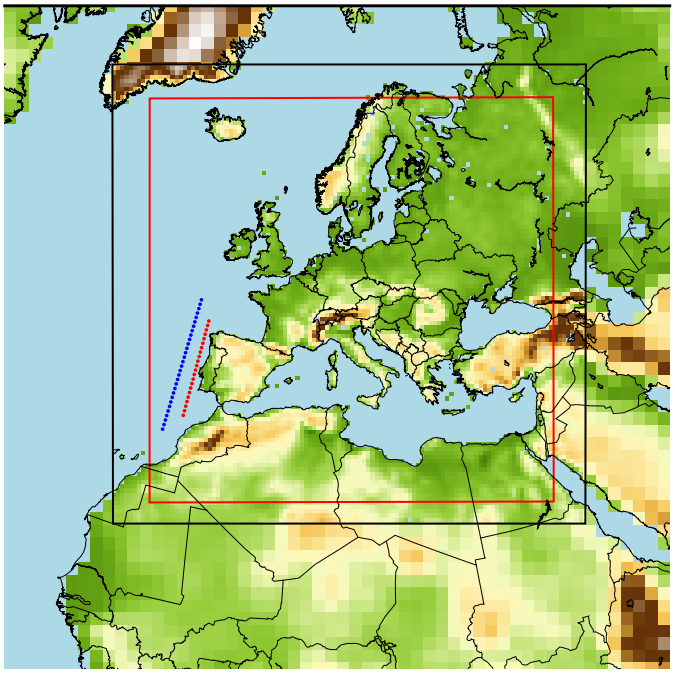

Figure 1. Spatial configuration of the three experiments, consisting of two one-way nested domains. The outer domain has a resolution of about 150 km and the inner Euro-CORDEX domain, which is boxed in black, has a resolution of 0.44°. The area between the black and red boxes approximately represents the blending area of the inner domain. Identification line 1 (red) consists of 22 equidistant points between 34°N and 44.5°N located at a longitude of -10°E. Identification line 2 (blue) consists of 30 equidistant points between 32°N and 46.5°N located at a longitude of -12°E.

AIRA is structured into two main blocks, with the first block encompassing data preprocessing and initial filtering, while the second block involves the identification and filtering of AR candidates and is subdivided into two stages. The first stage, Part A of the algorithm, determines the time intervals in which the IVT threshold has been consecutively exceeded. In the second stage, Part B, each of these intervals is evaluated against a set of conditions to determine whether an AR has been identified. Both blocks are elaborated upon in detail in the following subsections.

https://doi.org/10.5194/egusphere-2023-1155
Preprint. Discussion started: 6 July 2023

2.2.1 Data preprocessing

Figure 2 illustrates the data preprocessing stage of AIRA. First, the magnitude and direction of the IVT are bilinearly interpolated to the detection lines, L1 and L2, enabling the computation of the required variables. Next, the maximum IVT detected on L1, denoted as IVT_1, is identified for each time step t, and a first filter is applied to detect potential ARs. This filter sets a threshold value Γ for the IVT magnitude. If $IVT_1(t) \geq \Gamma$, then t is considered as a time step with a potential AR. At this time step t, AIRA also determines the latitude of the maximum IVT on L1, denoted as ϕ_1, and the direction of the IVT at that point, denoted as D. Additionally, AIRA computes the latitude of the minimum value of IVT on L1 that still exceeds the threshold, denoted as ϕ_{min}, and the latitude of the maximum value of IVT on L2, denoted as ϕ_2. This information is necessary to estimate the direction, d, and width, w, of the potential AR.

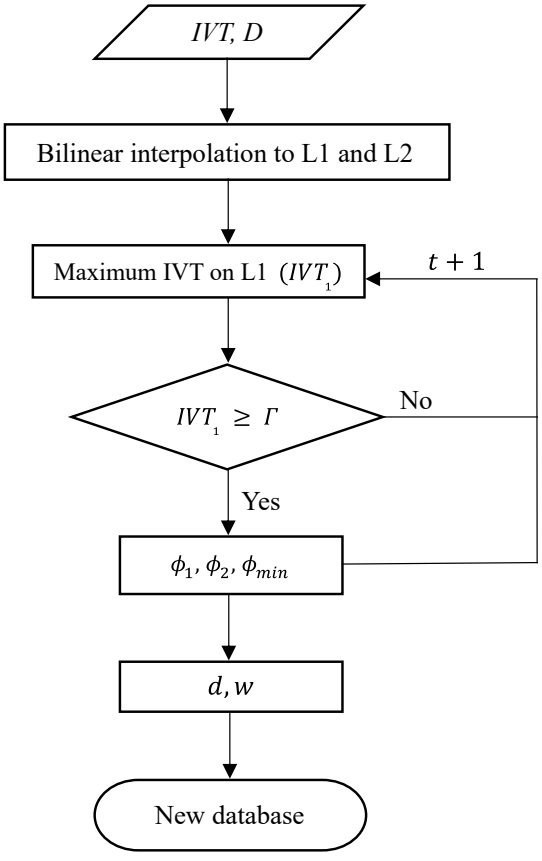

Figure 2. Diagram of the data preprocessing. The magnitude and eastward direction of the IVT are bilinearly interpolated to the detection lines. The maximum IVT on L1 is located for each time step and if it exceeds the established IVT threshold Γ, it is considered as part of an AR candidate. Thus, the maximum IVT, the latitudes of the IVT maximum and minimum, the IVT direction, the AR width and its direction through the lines are recorded in a new database.

https://doi.org/10.5194/egusphere-2023-1155
Preprint. Discussion started: 6 July 2023

The direction of the potential AR at time step t, denoted as d, can be computed using Equation 4, where ϕ_1 and ϕ_2 are the latitudes of the maximum IVT value on L1 and L2, respectively. The distance in kilometres corresponding to one degree of latitude is assumed to be constant at 111.20 km, while the equivalent distance for a degree of longitude varies with the latitude ϕ. The Earth radius is represented by R_T, and an average value of $R_T = 6371$ km is assumed. $\Delta\ell$ represents the longitude difference between the detection lines. All the trigonometric functions in the following equations are defined in sexagesimal degrees, resulting in d being obtained in degrees East.

$$d = \tan^{-1}\left(\frac{111.20(\phi_1 - \phi_2)}{\frac{\Delta\ell}{180}\pi R_T \cos\phi_2}\right) \tag{4}$$

The width of the potential AR is calculated under the assumption of its symmetry in section, meaning that the maximum is located at the center with equal distances to both lateral boundaries where the IVT threshold is still exceeded. Hence, the width detected on L1, a, expressed in degrees North, can be determined by using Equation 5. However, ARs usually do not pass through the detection lines with a perfectly perpendicular trajectory. As such, the actual width w of the potential AR that would be detected can be estimated using Equation 6.

$$a = 2|\phi_1 - \phi_{min}| \tag{5}$$

$$w = 111.20\ a\cos d \tag{6}$$

Finally, at each time step t, the date and time are associated with the values obtained for the variables of interest, namely IVT_t (the maximum IVT detected on L1), D, ϕ_1, ϕ_2, ϕ_{min}, d and w. These values are recorded in a new database. The procedure is then repeated for the next time step, and so on until the entire study period is covered. If $IVT_1(t) < \Gamma$, the current time step is skipped as an AR cannot be considered to be passing through L1, and the procedure moves on to the next time step until the entire study period is covered.

2.2.2 Identification and filtering: parts A and B

Part A of the algorithm involves delimiting the time intervals in which the maximum IVT magnitude exceeds the threshold value Γ consecutively (Figure 3 (left)). To accomplish this, the data obtained in the data preprocessing stage is augmented with the remaining time steps where $IVT_1(t) < \Gamma$, and all their variables are set to zero except for the date and time.

To characterize the different time intervals, two lists are employed, with one recording the beginning time steps and the other recording the ending time steps. Moreover, the possibility of consecutive arrivals of two atmospheric rivers is considered in the algorithm. If a significant shift (s) in latitude is detected between $\phi_1(t)$ and $\phi_1(t+1)$ an interval is considered to end and another to begin.

https://doi.org/10.5194/egusphere-2023-1155
Preprint. Discussion started: 6 July 2023

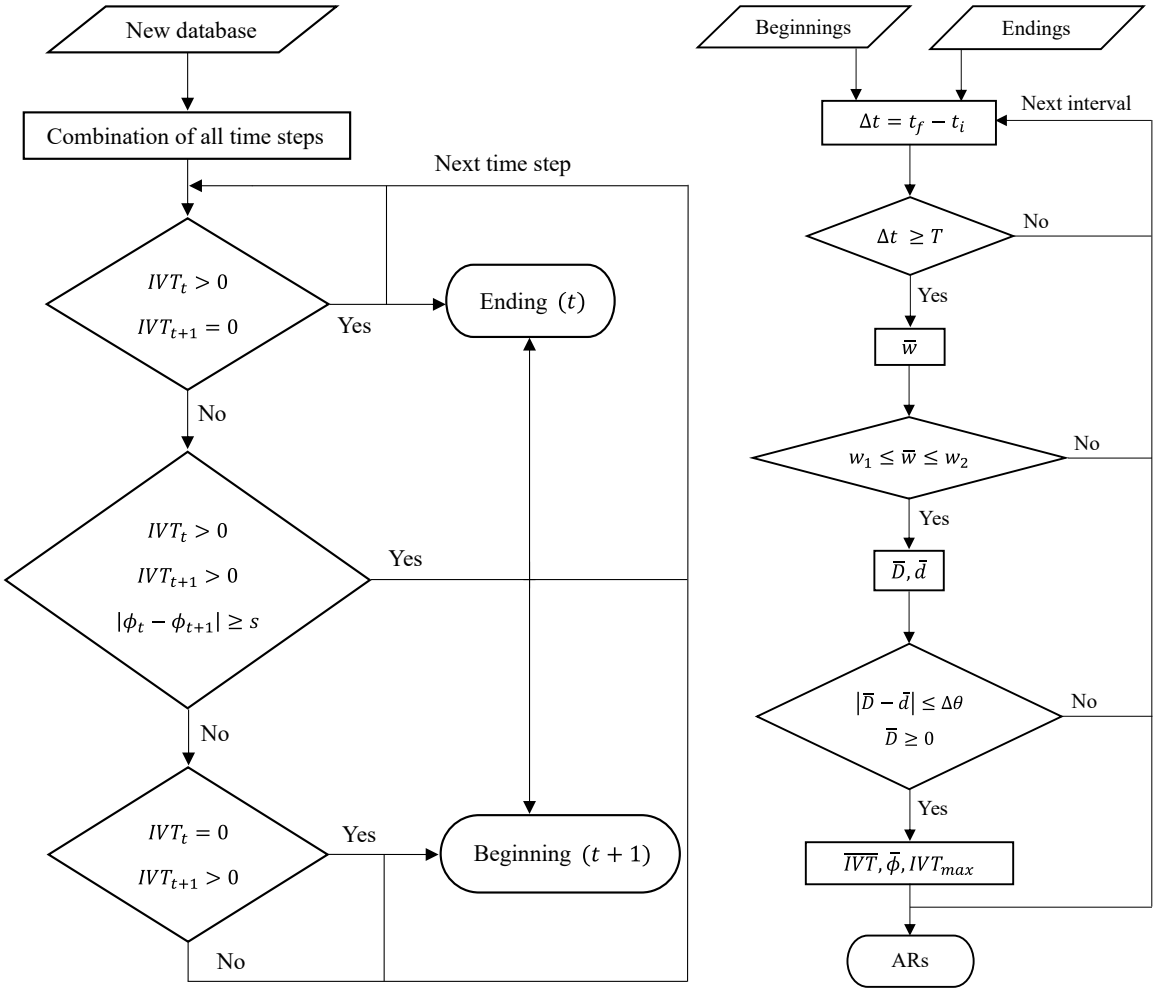

Figure 3. Diagram of AIRA. (Left) Part A. The database obtained in the data preprocessing is completed with the remaining time steps and the intervals candidate to AR are delimited with their beginning and ending. (Right) Part B. Each AR candidate interval is analysed separately. An AR is considered to be detected if the interval has at least a minimum duration, its average width is between a lower and upper limits and the direction of the IVT is positive and similar to the direction in which the potential AR passes through the detection lines. In the final database, each identified AR is recorded with 13 variables of interest.

https://doi.org/10.5194/egusphere-2023-1155
Preprint. Discussion started: 6 July 2023

Each interval obtained in Part A of the algorithm represents a potential AR. Part B of the algorithm (Figure 3 (right)) aims to determine whether these intervals meet a set of criteria to be considered as ARs. Firstly, the IVT threshold, Γ, must be exceeded on L1 for at least T consecutive time steps, which allows for the estimation of the AR length. Additionally, the average width of the potential AR, $\bar{w}$, must fall within the limits of w_1 and w_2 to ensure its filamentary structure. Moreover, the mean direction of the IVT, $\bar{D}$, must be positive and match the mean direction through the identification lines, $\bar{d}$, within a range of $\Delta\theta$, to ensure moisture transport is occurring. For the Southern Hemisphere, the condition for $\bar{D}$ changes to $\bar{D} \leq 0$, but both conditions can be disabled in the AIRA setup parameters. Finally, potential ARs with a mean latitude corresponding exactly to the limits of L1 are excluded since they occur outside the study domain.

The AR database obtained includes 13 variables, providing detailed information about each AR detected. For each AR, the database records the start and end date and time, the initial and final time-step indices, the number of time-steps Δt of the AR, its mean impact latitude ($\bar{\phi}$), the mean intensity ($\overline{IVT}$), the maximum intensity (IVT_{max}), the mean width ($\bar{w}$), the mean direction of the IVT ($\bar{D}$), and the mean direction of the AR passing through the detection lines ($\bar{d}$).

3 Results and discussion

3.1 AIRA implementation and application

To focus on ARs landfalling on the IP from the west, this study considered identification lines shown in Figure 1. L1, situated at a longitude of -10°E, is the nearest line to the Iberian west coast, comprising 22 points with latitude increasing from 34°N to 44.5°N in steps of 0.5°N. L2, on the other hand, has 30 points and is positioned at a longitude of -12°E, with the latitude range between 32°N and 46.5°N, also increasing by 0.5°N in steps.

Before implementing the algorithm, it is necessary to determine the values of the parameters involved (Table 1). Firstly, the mean of the 90th percentile of the IVT magnitude on L1 for all time steps resulted in a value close to 260 kg m^{-1} s^{-1} in all three experiments. To ensure the identification of ARs occurring in summer, a higher IVT threshold of Γ = 300 kg m^{-1} s^{-1} was selected. Secondly, the minimum time duration for an interval to be classified as an AR was set at T = 10 h. Given that the mean wind speed associated with ARs in the study area is around 30 m s^{-1}, this minimum duration would indicate the occurrence of an AR approximately 1,000 km in length. Another condition was established to ensure the filamentary structure of the ARs, which are long and narrow. Considering a minimum length of approximately 1000 km, it was established that the width of the ARs must be between $w_1 = 150$ km and $w_2 = 800$ km.

Table 1. Imposed values for the AIRA parameters: IVT threshold, Γ; latitude shift between two consecutive ARs, s; minimum interval duration, T; lower and upper width limits, w_1 and w_2, and maximum deviation between directions, $\Delta\theta$.

Γ (kg m^{-1} s−1)	s (°N)	T (h)	w_1 (km)	w_2 (km)	$\Delta\theta$ (°)
300	10	10	150	800	25

https://doi.org/10.5194/egusphere-2023-1155
Preprint. Discussion started: 6 July 2023

The application of AIRA to the three simulations (BASE, ARI and ARCI) resulted in three databases with the information of the identified ARs during the two decades from 1991 to 2010. In the reference experiment, BASE, a total of 244 ARs were detected. The AIRA algorithm identified 248 ARs in the ARI experiment and 250 ARs in the ARCI simulation. It was found that most of the ARs identified by AIRA also matched those identified by global-scale algorithms, as reported by Brands et al. (2017).

3.2 Climatology of the identified ARs

The number of ARs detected using AIRA is consistent across the three experiments, with between 5 and 15 ARs detected per year on average. However, there are exceptions to this pattern, such as in 1994 and 2007-2008, where the number of ARs is slightly lower. Furthermore, the total number of ARs identified per month exhibits a significant decline in July and August, but the number of detections increases in other seasons, particularly in spring and autumn. Notably, the highest number of ARs is detected in October, with at least 30 ARs identified in all three simulations (Figure 4 (top)).

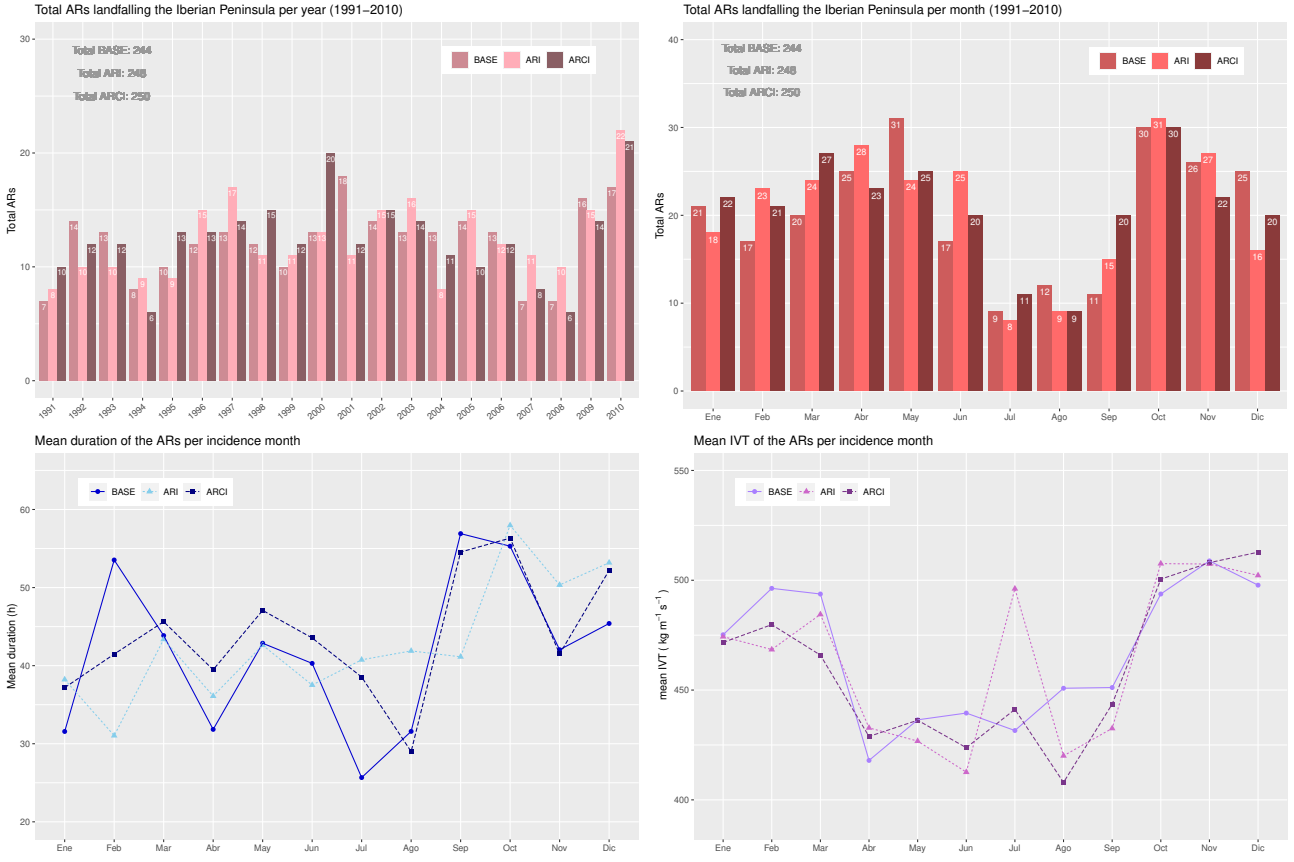

Figure 4. (Top) Histograms of the total ARs landfalling the IP per year (1991-2010) and per month in the three experiments. (Bottom) Mean duration and mean IVT magnitude of the ARs per month.

https://doi.org/10.5194/egusphere-2023-1155
Preprint. Discussion started: 6 July 2023

In addition, the mean duration of ARs varies depending on the month of occurrence, and it is observed to be longer than one day, approximately equivalent to 2,600 km, and in some cases, even longer than two days. September and October showed the most persistent ARs while the summer months had the shortest duration for ARCI and BASE. In ARI, the longest events took place in October and December, while the minimum duration occurred in February. The mean intensity of the identified ARs, which is the mean magnitude of the maximum IVT on L1, exhibits similar behavior to that of the duration for all three experiments. The least frequent, shortest, and weakest ARs occurred in the summer, while the most frequent, longest, and most intense ARs occurred in autumn (Figure 4 (bottom)).

The ARs identified by AIRA had an average width ranging from 200 to 500 km, with the highest frequency close to 200 km in BASE and ARCI, and close to 300 km in the ARI experiment. The majority of the ARs lasted between 10 and 50 hours, with the highest frequency around 20 hours. However, there were a few persistent events that lasted more than 170 hours. The ARs generally had a mean direction between 30° and 50°, with the highest frequency around 40°, though some cases of inclination less than 10° were also identified. The incidence of ARs was minimum above 36°N, with no clear maximum. Most of the identified ARs had a mean intensity between 320 and 500 kg m^{-1} s^{-1}, although some of them exceeded 700 kg m^{-1} s^{-1} on average. Additionally, the majority had a maximum IVT between 350 and 800 kg m^{-1} s^{-1}, with the highest frequency around 500 kg m^{-1} s^{-1}. However, some cases exceeding 1,200 kg m^{-1} s^{-1} were identified in all three simulations.

3.2.1 Associated ratio of the total precipitation

In order to estimate the percentage of total accumulated precipitation that could be related to the presence of ARs, the precipitation recorded on a given day was considered to be due to an AR if its presence has been detected in at least one hour of that day.

In all three simulations, it is apparent that the maximum percentage of total precipitation attributable to the presence of ARs is close to 30% and occurs along the western Iberian coast, which is the impact zone of the ARs (Figure 5). In Galicia (located in the northwest region of the IP), this percentage is slightly lower owing to the greater amount of precipitation that is not associated with ARs. The ARCI experiment exhibits the highest percentage for the entire domain, which can be attributed to the interactive introduction of various types and concentrations of aerosols acting as CCN in this simulation. Additionally, in maritime regions, aerosol concentrations are lower than over land, and highly hygroscopic aerosols predominate. Consequently, droplets grow more rapidly, resulting in increased precipitation (Pravia-Sarabia et al., 2022).

3.3 Common AR events

To study the potential differences between the ARs of the three experiments, their common AR intervals have been identified and compared. Only 37% of the time steps with ARs coincide among all three simulations concerning the BASE total. This low percentage could be attributed to weak events and the temporal limitations of the identified ARs, where the IVT threshold is exceeded in some simulations but not in others. Furthermore, aerosol effects can cause spatial deviations, as seen in the following sections, potentially pushing ARs out of the study area, decreasing the time steps with AR on the detection lines in some experiments, and thus lowering the coincidence percentage. The AIRA algorithm was applied to these common time

https://doi.org/10.5194/egusphere-2023-1155
Preprint. Discussion started: 6 July 2023

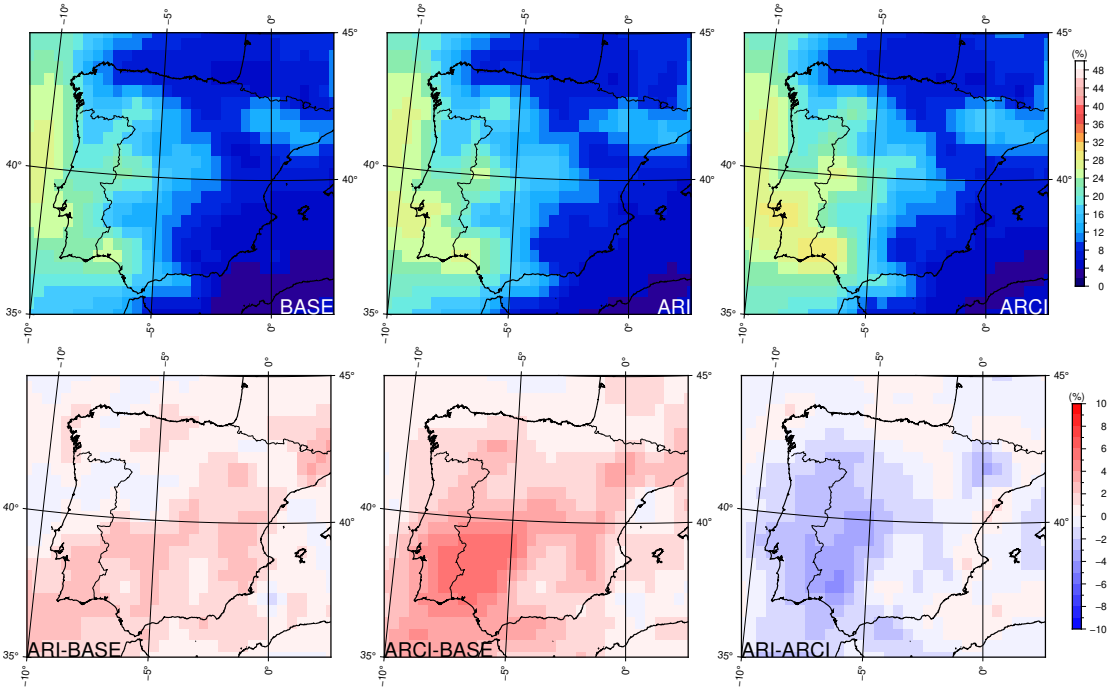

Figure 5. (Top) Percentage of total precipitation explained by the influence of ARs in each simulation for the period 1991-2010 and (bottom) differences between simulations.

steps, eliminating coincident intervals with a duration of less than 10 hours or not satisfying the other criteria to be deemed proper ARs. As a result, a total of 80 common AR intervals from the three experiments were obtained, and their characteristics were compiled. The fewest number of common events occurred in summer, with only one occurrence in July or August, while the most frequent events occurred in March (13 intervals) and October (11 common AR events).

3.3.1 Analysis of the differences

The common AR events from the three simulations show that there are no significant deviations between the ARs in the strongest events. However, some differences are observed in the mean direction and impact latitude of the ARs in other cases. To investigate this further, the ARI-BASE and ARCI-BASE differences of the mean IVT direction, mean impact latitude, and mean IVT magnitude were plotted against the maximum IVT (Figure 6). The maximum IVT was obtained by averaging the maximum IVT magnitude of each AR event in the three experiments. The spatial deviations tended to zero, and the ARI-ARCI differences in the three magnitudes considered became minimal in the most intense events.

https://doi.org/10.5194/egusphere-2023-1155
Preprint. Discussion started: 6 July 2023

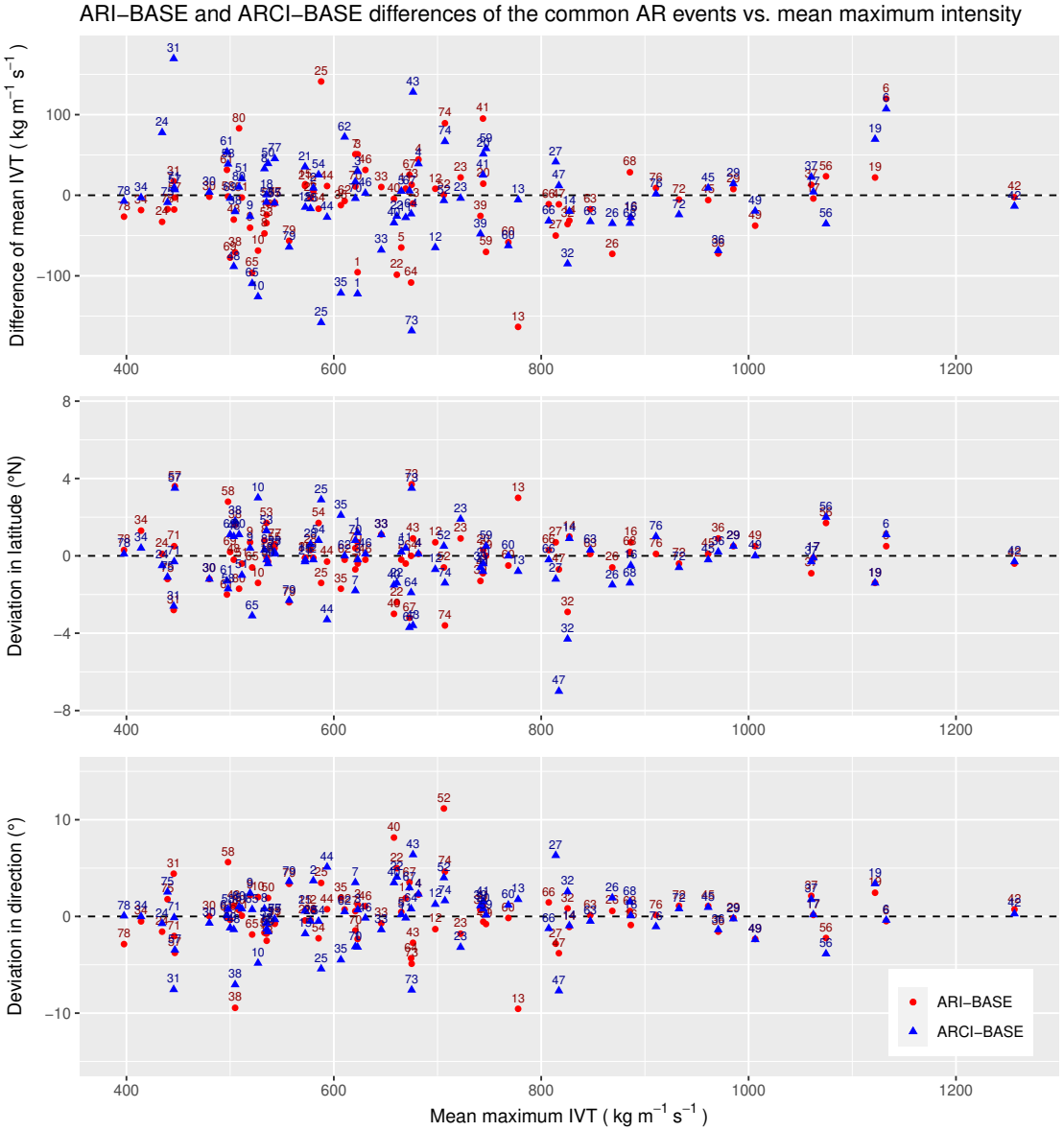

Figure 6. ARI-BASE (red) and ARCI-BASE (blue) differences in mean IVT direction, mean impact latitude and mean intensity (IVT magnitude) of the common AR events vs. their maximum intensity.

https://doi.org/10.5194/egusphere-2023-1155
Preprint. Discussion started: 6 July 2023

3.3.2 Spatial aerosol loading and ARs modification

To understand the influence of aerosols on the observed spatial deviations and IVT differences of the ARs, a classification and analysis of the common events have been carried out based on the spatial loading of the most relevant aerosols present in the study area, namely dust and sea salt. Initially, an EOF analysis has been jointly performed for the sea salt and dust AOD (550 nm) standardised anomalies within the region bounded by -15°E and 4°E longitude and 33°N and 45°N latitude. The ARI and ARCI experiments used five and six EOFs respectively, explaining 75% of each total variance. A clustering classification was then performed on these analyses, which separated the common cases into eight different groups. The centroid of each cluster was associated with two centre fields, one per considered aerosol.

Figure 7 displays the two centres (sea salt and dust) of the eight ARI clusters, which were obtained as the mean fields of the events belonging to each group. The first clusters present a higher dust aerosol loading, while the latter ones exhibit a more significant loading of sea salt. Figure 8 shows the ARI-BASE IVT differences of each ARI group. Focusing on the groups that have more than one event and present the most significant differences, it was observed that an AR weakening occurs in clusters 2 and 3. The high concentration of mineral aerosols over the IP may be the reason for this weakening. In contrast, the sea salt aerosols have very low presence in both groups, and their effects are expected to be small and thus negligible.

ARs are commonly associated with a frontal surface, which can be identified by analyzing the thickness field. The thickness field shows the maximum temperature gradient and thus the position of the front, which guides the AR. Moreover, stronger thickness gradients lead to more intense ARs. The mean thickness fields between 1,000 and 850 hPa of the events belonging to ARI clusters 2 and 3 are represented in Figure 9 for ARI and BASE experiments. The same time steps are included in the representations of both experiments. As observed in cluster 2, the cooling effect caused by aerosol-radiation interactions of dust results in weaker thickness gradients in the warmer zones when compared to BASE. In cluster 3, a wider cooling effect is present, but the more pronounced cooling in the south (over the north of Africa) leads to the observed weakening.

On the other hand, clusters 2 and 3 of the ARI experiment also exhibit some spatial deviations, as shown in Figure 8. However, they exhibit opposite behaviors. The comparison of latitude and direction differences of the entire set of common events yields a significant negative correlation factor of -0.62, indicating that the aerosol configurations associated with northward (southward) deviations could also be linked to changes in the mean direction, resulting in more zonal (meridional) ARs relative to the BASE simulation.

An analogous analysis was employed to investigate the ARCI-BASE differences. The center fields of each ARCI dust and sea salt cluster are depicted in Figure 10, which were computed as the mean fields. As before, the first clusters are characterized by a higher concentration of dust, whereas the last ones exhibit a higher presence of sea salt aerosols. The integration of the direct, semi-direct, and indirect effects of these aerosols causes a significant strengthening of the ARs associated with clusters 2 and 6, and a considerable weakening of the events belonging to clusters 7 and 8, as illustrated in Figure 11.

To understand the influence of aerosol interactions on the mean integrated vapor transport (IVT) magnitude of ARs, the thickness field of the clusters that exhibited the greatest ARCI-BASE differences was analyzed, as shown in Figure 12. Specifically, the presence of dust aerosols was found to be associated with warming of the atmospheric layer compared to the BASE

https://doi.org/10.5194/egusphere-2023-1155
Preprint. Discussion started: 6 July 2023

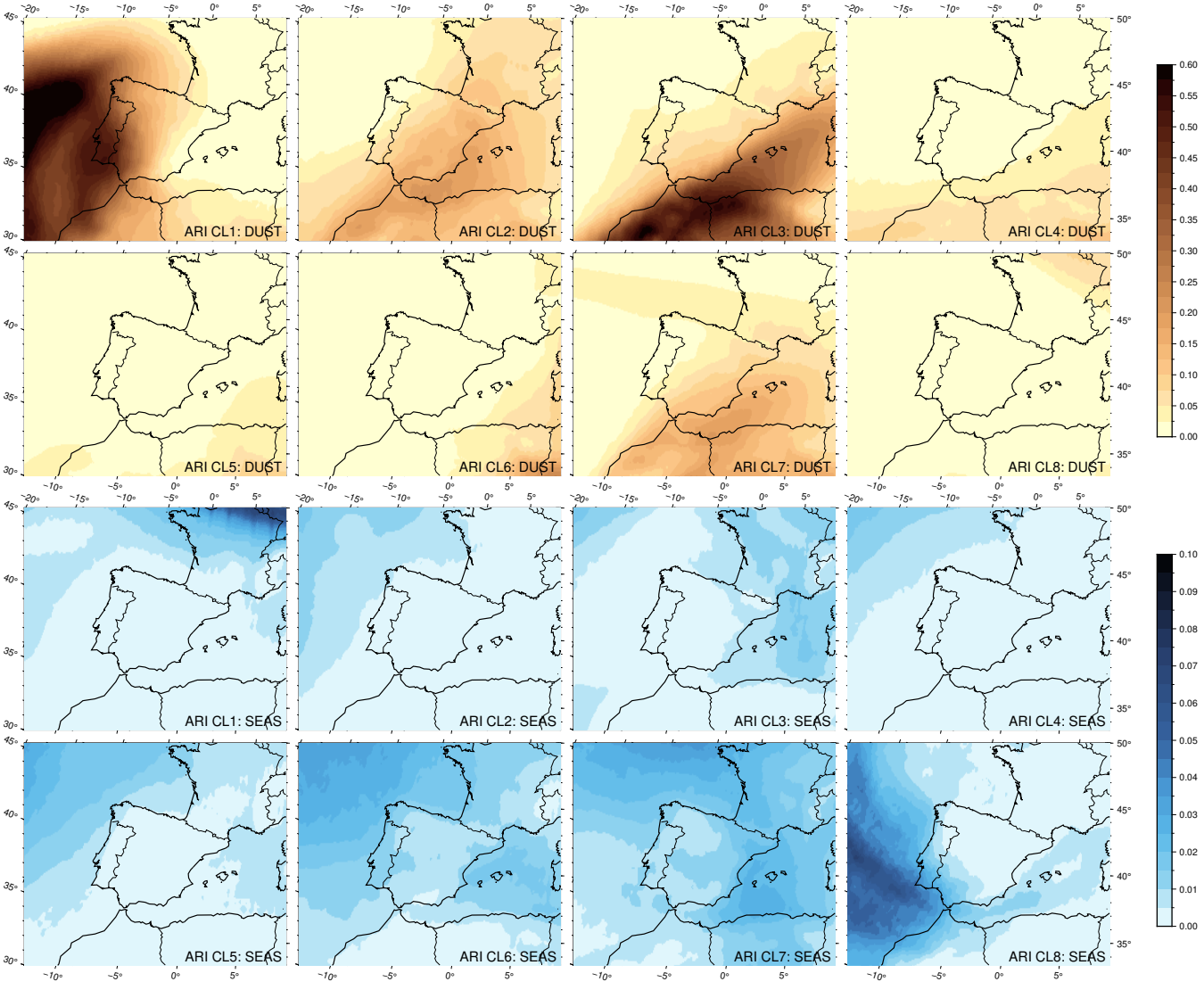

Figure 7. Centres of dust (DUST) and sea salt (SEAS) AOD at 550 nm of the different ARI clusters (CL).

https://doi.org/10.5194/egusphere-2023-1155
Preprint. Discussion started: 6 July 2023

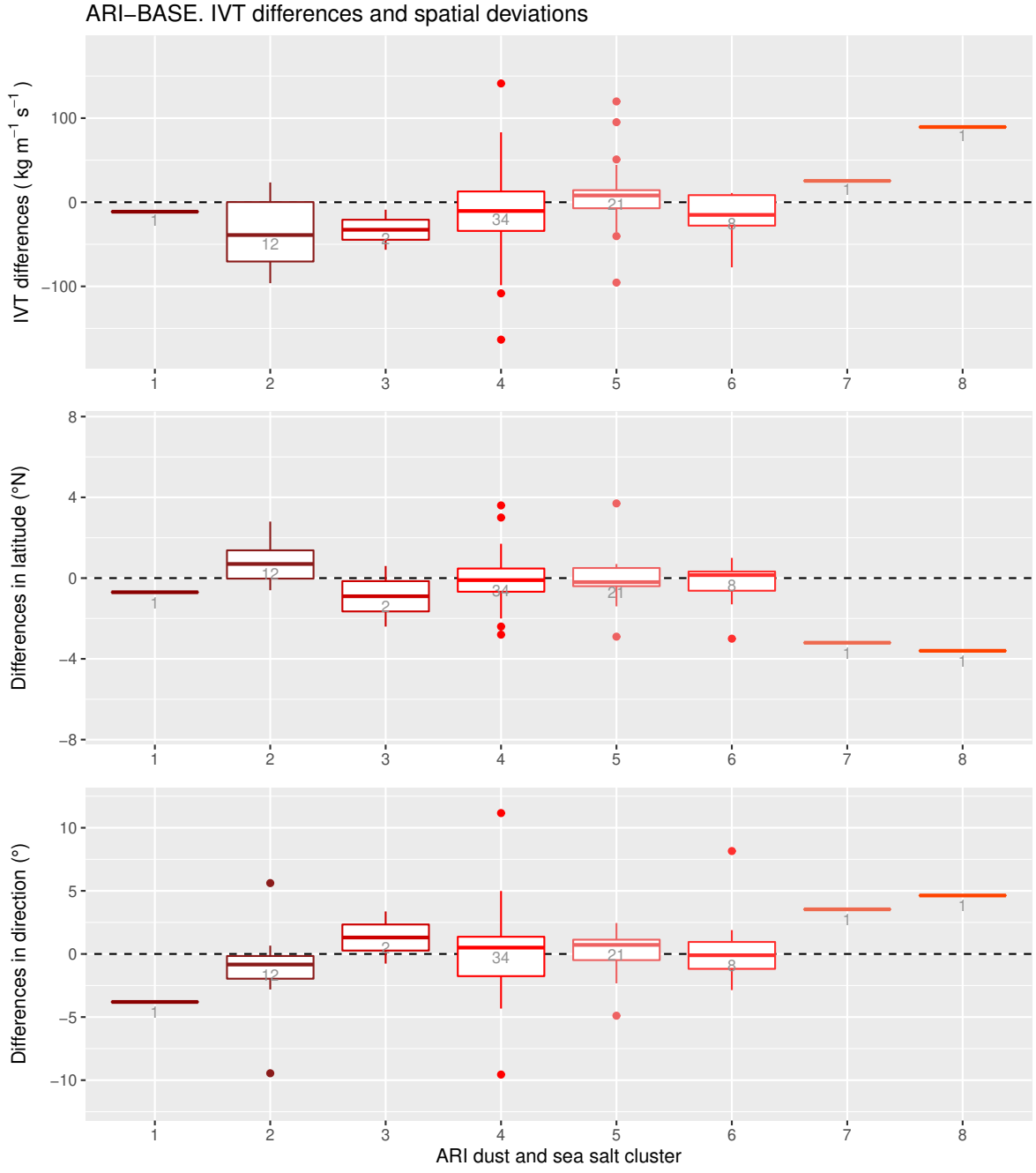

Figure 8. ARI-BASE differences of the mean IVT magnitude, mean incidence latitude and mean IVT direction of the common AR intervals grouped by the eight ARI sea salt and dust cluster groups. The number of events belonging to each cluster is indicated in grey.

https://doi.org/10.5194/egusphere-2023-1155
Preprint. Discussion started: 6 July 2023

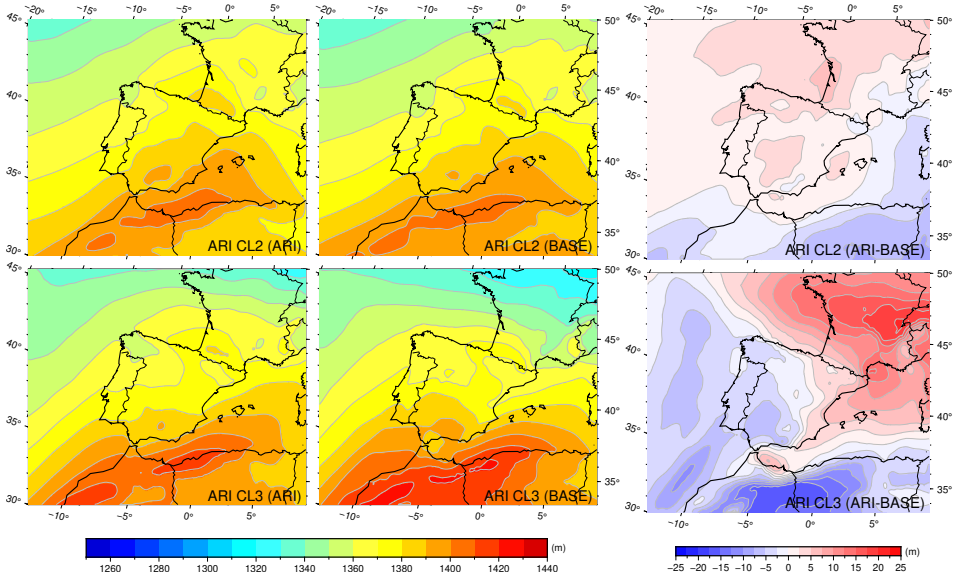

Figure 9. ARI and BASE mean thickness fields of the atmospheric layer between 1,000 and 850 hPa of the common AR events belonging to clusters 2 and 3 in the ARI simulation and ARI-BASE thickness differences. The same time steps are included in the representations of both experiments.

case, primarily due to indirect effects. High concentrations of dust aerosols generate a large number of small droplets that lead to increased cloud lifetime and warming of the atmospheric layer due to the release of latent heat. This effect is evident in cluster 2, where the positive differences align well with the distribution of dust. Furthermore, this warming of the warm zones leads to the strengthening of the thickness gradient, resulting in increased mean IVT magnitude of the ARs associated with this aerosol configuration.

Clusters 6, 7, and 8 are characterized by higher concentrations of sea salt aerosols, and their interactions with the atmosphere become relevant. Sea salt aerosols are highly hygroscopic and lead to a cooling effect on the atmospheric layer when interacting with it. This is due to enhanced rain droplet formation and early precipitation, which reduces the release of latent heat. When combined with the effects of dust aerosols, the ARCI-BASE thickness differences observed in Figure 12 emerge. In cluster 6, the more significant cooling effect over the east of the IP than over the southeast results in a strengthening of the thickness gradient due to the higher concentration of sea salt aerosols. The particularly strong cooling observed over the north of the African continent may be attributed to the near-absence of sea salt and dust aerosols, which remarkably reduces the release of latent heat associated with droplet formation when compared to the BASE experiment (fixed concentration of CCN). On the other hand, cluster 7's common events, with a mean incidence latitude to the north, are primarily influenced by sea salt aerosols, which generate a wide but slight cooling in this configuration. Even subtle differences in the strength of this cooling may result in the observed weakening of the thickness gradient that guides the ARs. In a similar vein, weakened thickness

https://doi.org/10.5194/egusphere-2023-1155
Preprint. Discussion started: 6 July 2023

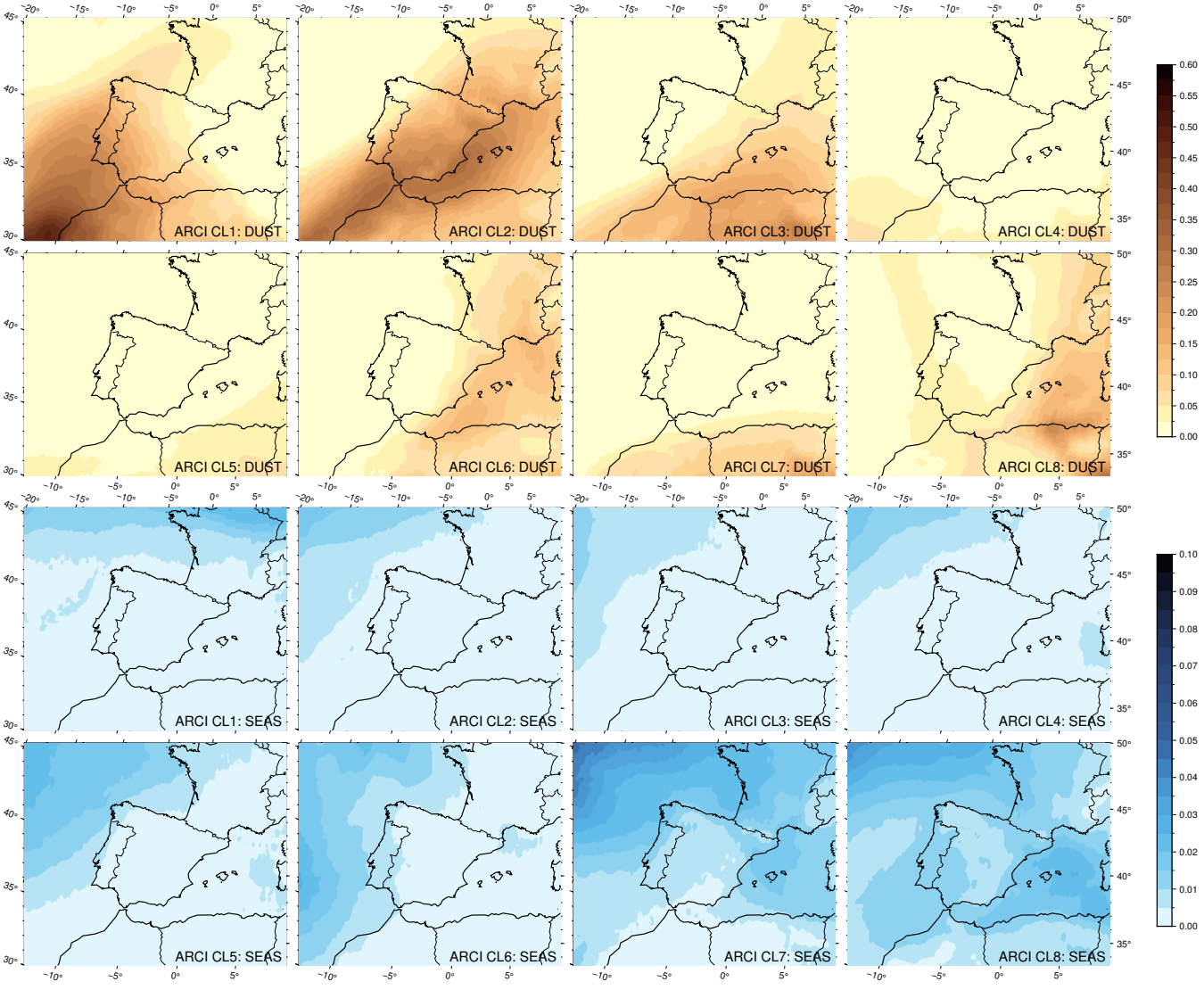

Figure 10. Centres of dust (DUST) and sea salt (SEAS) AOD at 550 nm of the different ARCI clusters (CL).

https://doi.org/10.5194/egusphere-2023-1155
Preprint. Discussion started: 6 July 2023

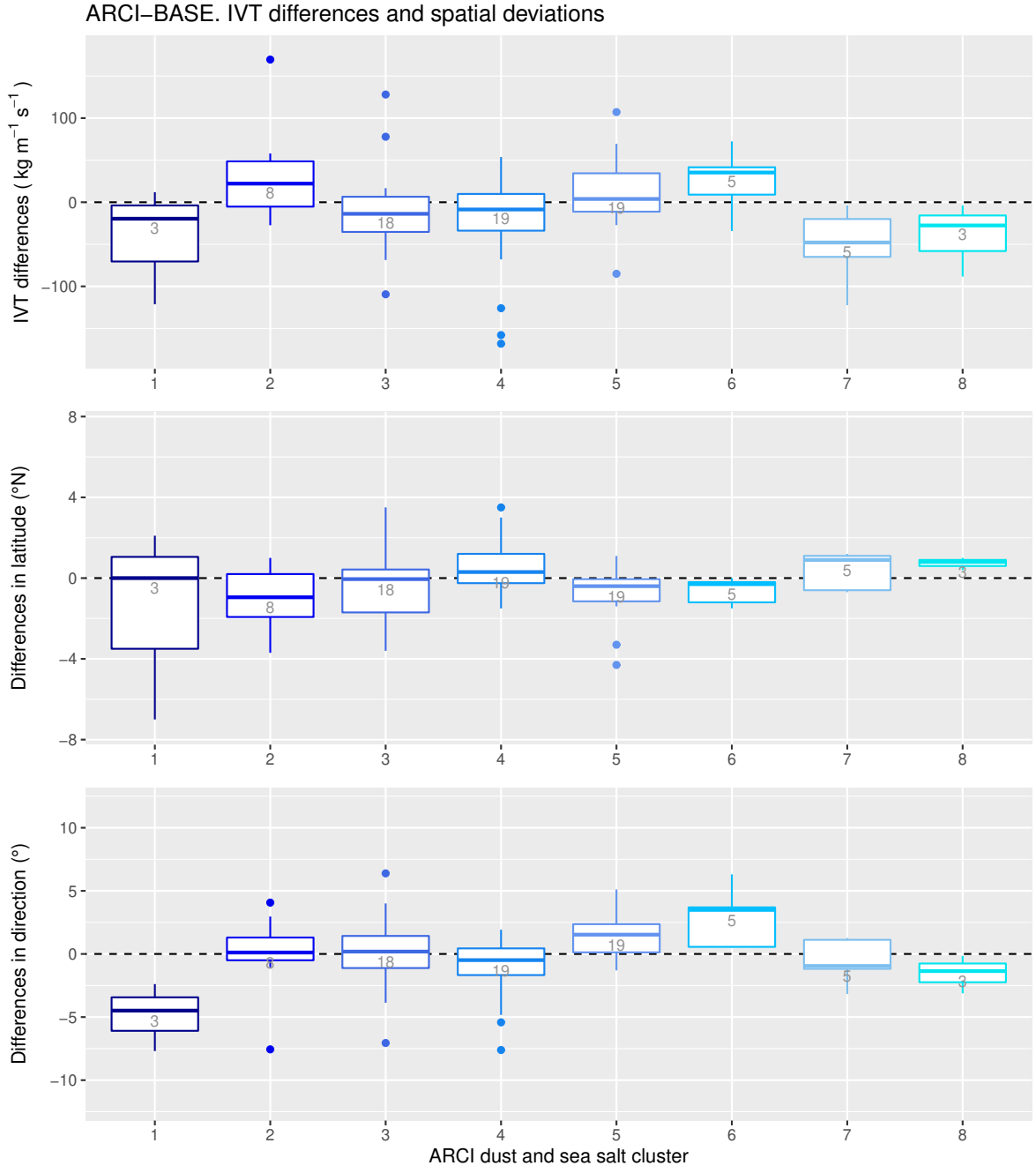

Figure 11. ARCI-BASE differences of the mean IVT magnitude, mean incidence latitude and mean IVT direction of the common AR intervals grouped by the eight ARCI sea salt and dust cluster groups. The number of events belonging to each cluster is indicated in grey.

https://doi.org/10.5194/egusphere-2023-1155
Preprint. Discussion started: 6 July 2023

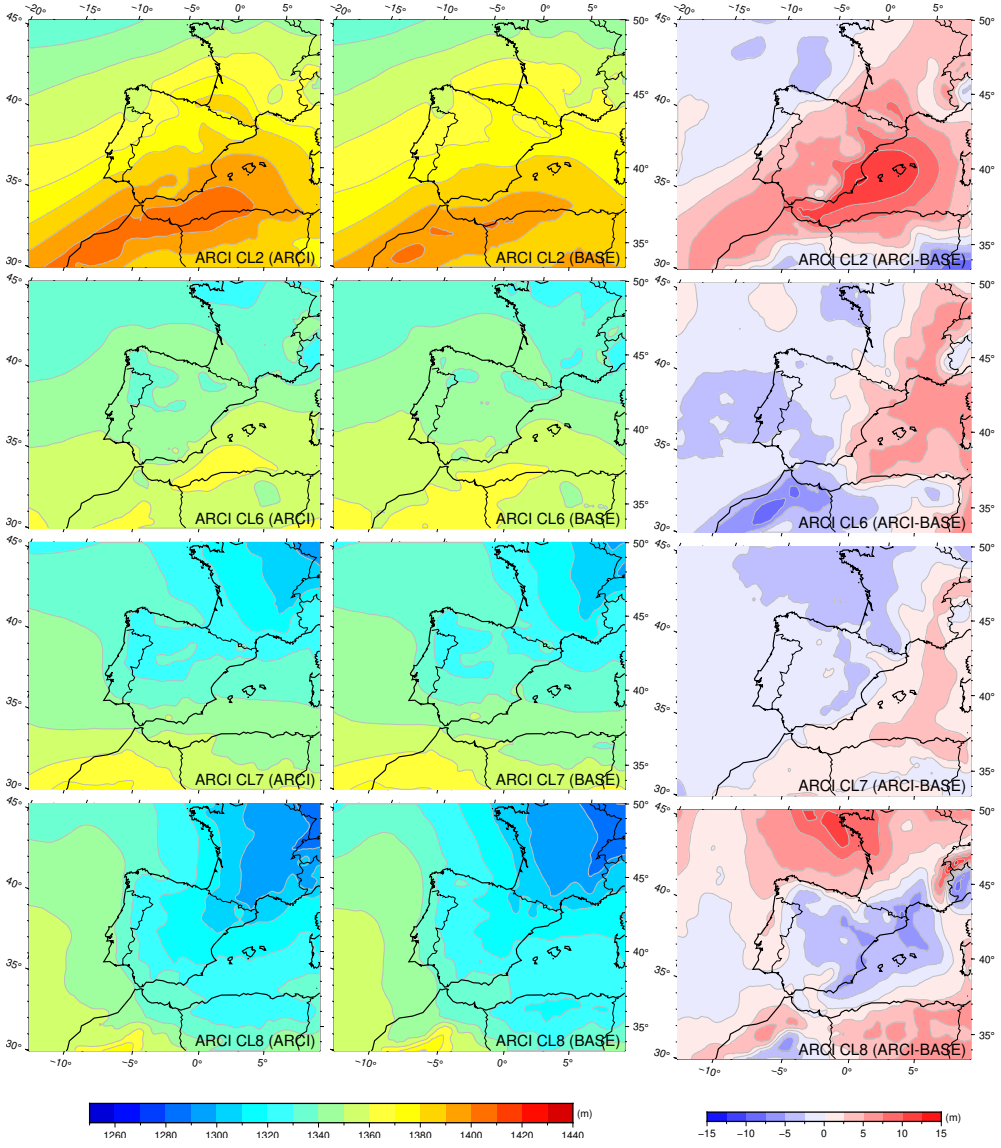

Figure 12. ARCI and BASE mean thickness field of the atmospheric layer between 1000 and 850 hPa of the common AR events belonging to clusters 2, 6, 7 and 8 in the ARCI simulation and ARCI-BASE thickness differences. The same time steps are included in the representations of both experiments.

https://doi.org/10.5194/egusphere-2023-1155
Preprint. Discussion started: 6 July 2023

gradients and ARs result in cluster 8, due to warming of the cold northern zones and slight cooling of the warm zones of the southeast of the IP.

Furthermore, similar to the ARI-BASE analysis, the comparison between latitude and direction differences of the entire set of common events in the ARCI-BASE experiment (Figure 11) resulted in a significant negative correlation factor of -0.43.

3.3.3 Case studies: 27th October 2005 and 12th January 1998

The application of clustering analysis and mean fields has provided valuable insights into the mechanisms underlying the perturbations of ARs by aerosols. Nonetheless, two case studies that compare the BASE, ARI and ARCI simulations can offer further insights into the role of aerosols in modifying ARs, while avoiding any potential smoothing effect of the mean fields. Specifically, the common AR events of 27th October 2005 (belonging to cluster 2 in both ARI and ARCI experiments) and 12th January 1998 (belonging to cluster 2 in the ARI experiment and cluster 6 in the ARCI experiment) were selected for analysis in these two case studies.

In the first case (Figures 13 and 14), ARI and ARCI ARs present a mean intensity difference of -70.32 and 58.01 kg m^{-1} s^{-1} with respect to the BASE AR, respectively. The IVT differences observed in the ARI simulation may be attributed to a cooling of the southwestern region of the study domain caused by dust aerosols, resulting in a weakening of the thickness gradient. On the other hand, the opposite occurs in the ARCI simulation, with a strong heating of the warm eastern zones and a slight cooling of the cold northern zones with respect to the BASE, resulting in a strengthening of the thickness gradient of the front that drives the AR. In the ARCI experiment, the indirect effects of dust particles in high concentration result in a larger number of small droplets, and the increased cloud lifetime leads to a greater release of latent heat, thereby causing a heating of the atmospheric layer. Moreover, the ARCI AR exhibits a more zonal direction (and a slight northward displacement, as expected from the results of the previous subsection), with the maximum temperature gradient and the frontal surface that guides the AR coinciding with the area of the highest dust AOD gradient. These temperature variations and circulation changes give rise to the observed IVT differences and the deviation of the detected AR.

Regarding the event on 12th January 1998 (Figure 15 and 16), both ARI and ARCI ARs show a mean intensity difference of -50.04 and 41.54 kg m^{-1} s^{-1} with respect to the BASE AR, respectively. The cooling effect of dust aerosols in the ARI simulation could be responsible for the weakening of the temperature gradient and the observed negative IVT differences. In contrast, the indirect effects of dust aerosols in the ARCI experiment result in a heating effect, and a further southward deviation of the AR trajectory. Although the ARCI AR shows a more zonal direction during the represented time-step, the whole interval has a mean direction 6.3° higher than in the BASE experiment (with an increased relative meridional component). The southward displacement of the sea salt distribution in the ARCI experiment coincides with the deviation of the AR trajectory.

In BASE and ARI experiments, the same types and concentrations of CCN are prescribed for both marine and continental areas. However, marine aerosols, primarily sea salt, are more hygroscopic and occur in lower concentrations compared to continental aerosols. As a result, larger and more rapidly precipitating droplets are formed, releasing less latent heat in the ARCI simulation, where aerosol effects on condensation are considered interactively. This decrease in the released latent heat leads to cooling of the cold zones relative to the BASE experiment, moving the maximum temperature gradient further south,

https://doi.org/10.5194/egusphere-2023-1155
Preprint. Discussion started: 6 July 2023

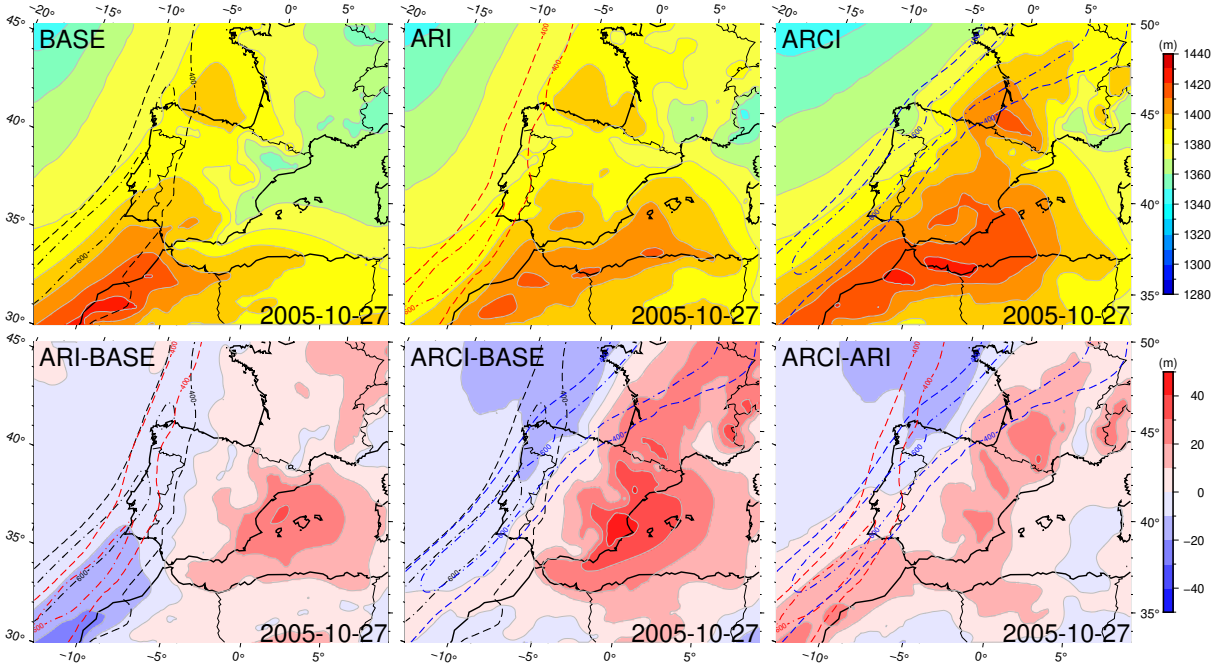

Figure 13. 22:00h, 27th October 2005. Thickness field between 1000 and 850 hPa of the three simulations (top) and thickness differences (bottom). Black, red and blue contours show BASE, ARI and ARCI ARs respectively (400 and 600 kg m^{-1} s^{-1} IVT levels).

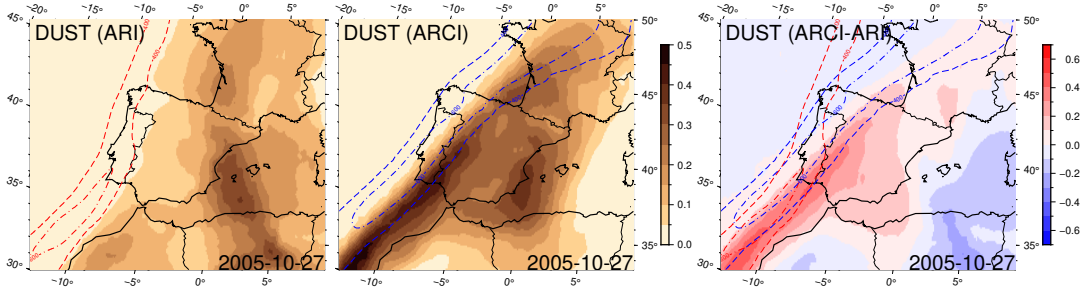

Figure 14. 22:00h, 27th October 2005. ARI and ARCI dust AOD at 550 nm and ARCI-ARI AOD differences. Red and blue contours show ARI and ARCI ARs respectively (400 and 600 kg m^{-1} s^{-1} IVT levels).

https://doi.org/10.5194/egusphere-2023-1155
Preprint. Discussion started: 6 July 2023

and coinciding with the southern border of the sea salt distribution. The combination of sea salt and dust aerosol indirect effects gives rise to a strengthening of the ARCI AR.

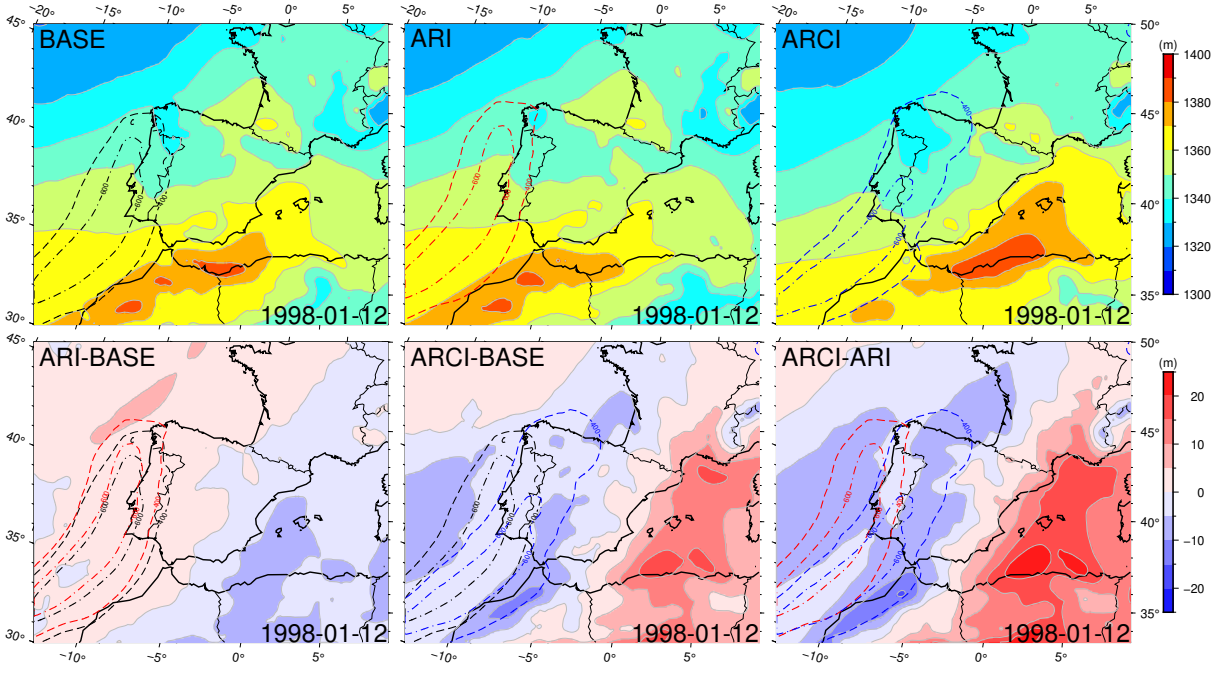

Figure 15. 09:00h, 12th January 1998. Thickness field between 1000 and 850 hPa of the three simulations (top) and thickness differences (bottom). Black, red and blue contours show BASE, ARI and ARCI ARs respectively (400 and 600 kg m^{-1} s^{-1} IVT levels).

4 Conclusions

ARs, which are associated with numerous extreme precipitation events in regions influenced by maritime flows, are of critical importance in meteorological predictions and climate change projections, both globally and regionally. The primary objective of this research was to investigate the sensitivity of ARs to aerosol treatment in regional climate simulations for the IP. To achieve this objective, ARs in three experiments that covered Europe during the period of 1991-2010 were analyzed. In the BASE experiment, aerosols were prescribed without considering their interactions with radiation, and the number of CCN was fixed. In contrast, in the ARI and ARCI experiments, the model resolved aerosols dynamically. The ARI experiment considered only the direct and semi-direct effects of aerosols, while the ARCI experiment included indirect effects as well.

A number of AR identification algorithms are available, but many of them are not suited for use with regional models. Therefore, a novel regional scale AR identification algorithm, called AIRA, has been developed based on IVT, which comprises two stages: 1) preprocessing and 2) filtering/identification. Initially, an IVT threshold is set, and the time intervals where the maximum IVT magnitude exceeds this threshold are identified. Subsequently, each time interval is assessed to determine if

https://doi.org/10.5194/egusphere-2023-1155
Preprint. Discussion started: 6 July 2023

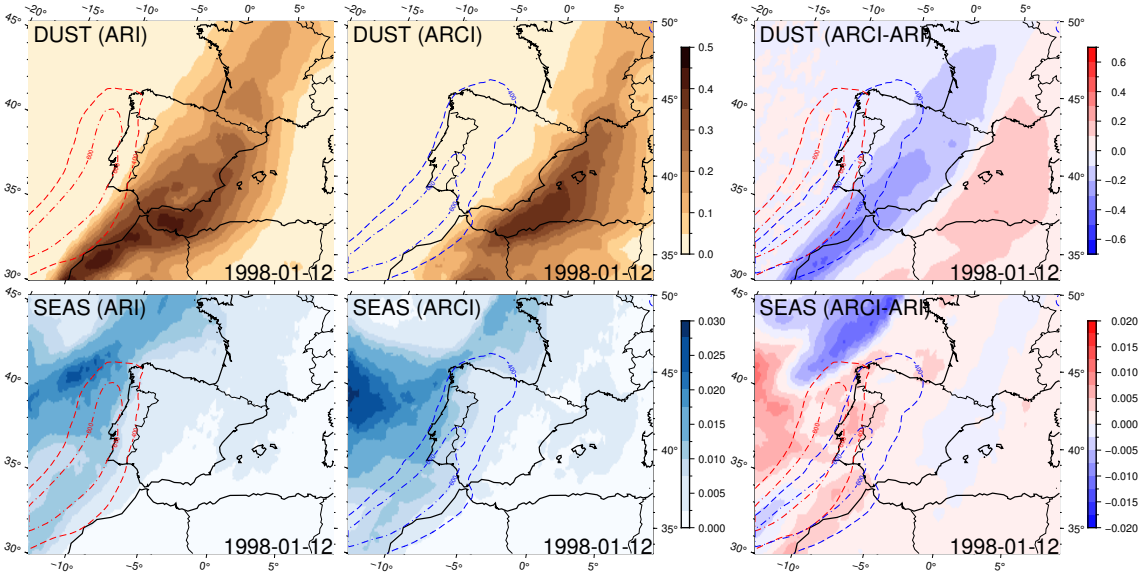

Figure 16. 09:00h, 12th January 1998. ARI and ARCI dust (top) and sea salt (bottom) AOD at 550 nm and ARCI-ARI AOD differences. Red and blue contours show ARI and ARCI ARs respectively (400 and 600 kg m^{-1} s^{-1} IVT levels).

it meets the necessary geometry conditions (length and width) and direction requirements to be identified as an AR. AIRA's performance was evaluated by comparing the results with a global algorithm archive of identified ARs.

AIRA successfully identified approximately 250 ARs in each experiment spanning the period from 1991-2010. Notably, the most frequent, intense, and long-lasting ARs occurred during spring and autumn, while they were less frequent, shorter, and weaker in the summer season. The direction of the axis of the identified ARs was observed to be distributed around 40°, indicating their transport from the tropical regions of the Atlantic Ocean. Furthermore, it was found that ARs were responsible for up to 30% of the total accumulated precipitation, underscoring the extreme nature of the precipitation associated with these events. Interestingly, the inclusion of aerosols, particularly their indirect effects, led to a redistribution of precipitation, with notable increases in the areas of occurrence.

Although the number of identified ARs is comparable among the three simulations, they were only observed simultaneously in 37% of the time steps with AR. This suggests that the inclusion of aerosols at different levels in the simulations may play a crucial role in determining their behavior. Comparison of the ARI-BASE and ARCI-BASE differences revealed that the deviations were minimal in the most intense cases, while the largest differences were observed in weaker events.

The joint analysis and classification of dust and sea salt aerosol distributions enabled the identification of eight main aerosol configurations in both ARI and ARCI simulations. In the ARI experiment, the aerosol-radiation interactions of dust resulted in a cooling effect. In contrast, dust was associated with a warming effect in the ARCI simulation, where the aerosol-cloud interactions of sea salt led to a cooling effect with respect to the BASE experiment. The combined action of dust and sea salt aerosols, through their direct and/or indirect effects, strengthened (weakened) the frontal surfaces guiding ARs by producing

https://doi.org/10.5194/egusphere-2023-1155
Preprint. Discussion started: 6 July 2023

a cooling (warming) of the cold zones and/or a warming (cooling) of the warm areas. The physical mechanisms underlying the modification of the dynamical conditions driving ARs were related to differences in the temperature gradient, which led to significant changes in the thickness field. These differences were associated with aerosol-radiation-cloud interactions, including direct, semi-direct and indirect effects, which were found to be relevant. Furthermore, a negative correlation was observed between mean direction and mean latitude differences. Specifically, deviations towards the north (south) were associated with more zonal (meridional) ARs with respect to the reference simulation.

In summary, this study has highlighted the impact of varying aerosol treatments on the simulation of ARs in regional climate models. Future research could examine the sensitivity of the outcomes to alterations in the different parameters employed by AIRA. Moreover, it would be worthwhile to explore whether incorporating more complex and computationally-intensive processes in the models would lead to notable enhancements in the representation of real AR events.

Code and data availability. The code developed to build AIRA is fully available as an open-access resource (https://doi.org/10.5281/zenodo.7885383, Raluy-López et al. (2023b)) on the Zenodo archive. The final product consists on a preprocessing bash script meant to be followed by the main part of the algorithm implemented with R functions. Figures have been prepared with R and Generic Mapping Tools (GMT) software. All the WRF-Chem simulations presented in this paper have been carried out in the MAR group of the University of Murcia as a product of the REPAIR project. The simulation output data used to generate figures presented throughout this paper are available as an open-access resource (https://doi.org/10.5281/zenodo.7898400, Raluy-López et al. (2023a)) on the Zenodo database.

Author contributions. ERL wrote the algorithm code, and performed the calculations in this paper. JPM contributed to the design of the simulations and their analysis. He also provided ideas for new approaches in the analysis of the simulations that have been integrated into the final paper. PJG and JPM provided substantial expertise for a deep understanding of the AR concept, which led to a successful conception of the algorithm. The manuscript writing has been led by ERL, with all authors contributed to reviewing the text.

Competing interests. The authors declare no conflict of interest.

Acknowledgements. The authors acknowledge the ECCE project (PID2020-115693RB-I00) of the Ministerio de Ciencia e Innovación/Agencia Estatal de Investigación (MCIN/AEI/10.13039/501100011033). ERL thanks her predoctoral contract FPU to the Ministerio de Universidades of Spain.

Appendix A: Correlation between latitude and direction differences

https://doi.org/10.5194/egusphere-2023-1155
Preprint. Discussion started: 6 July 2023

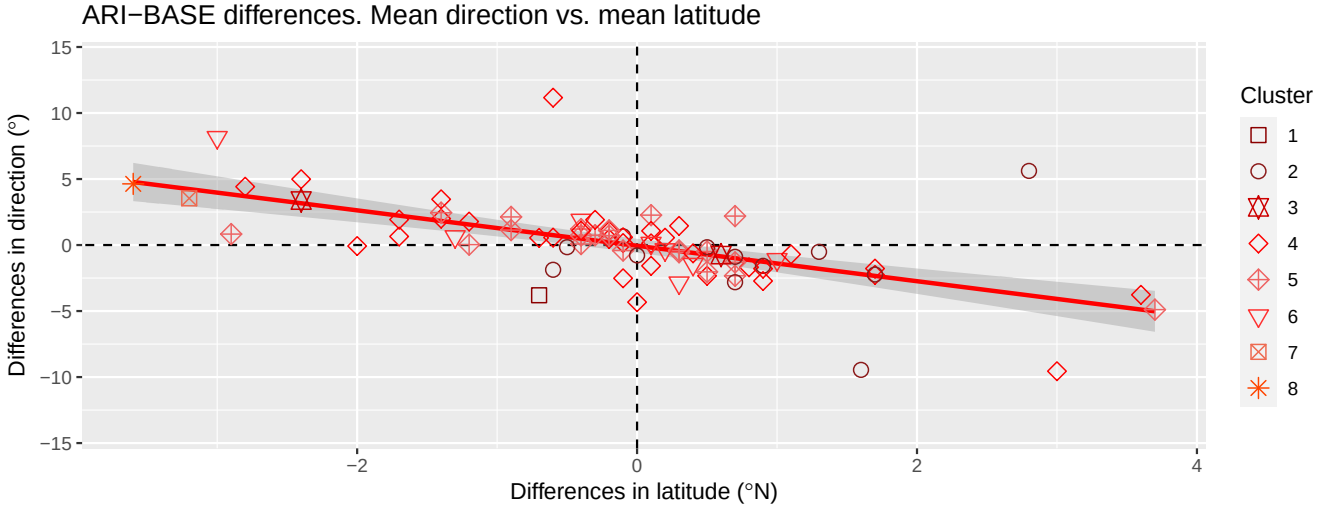

Figure A1. ARI-BASE differences in mean direction versus ARI-BASE differences in mean incidence latitude. Each set of shape and colour represents an ARI cluster. The linear regression model is plotted with a red line and the grey area represents the 95% confidence level interval.

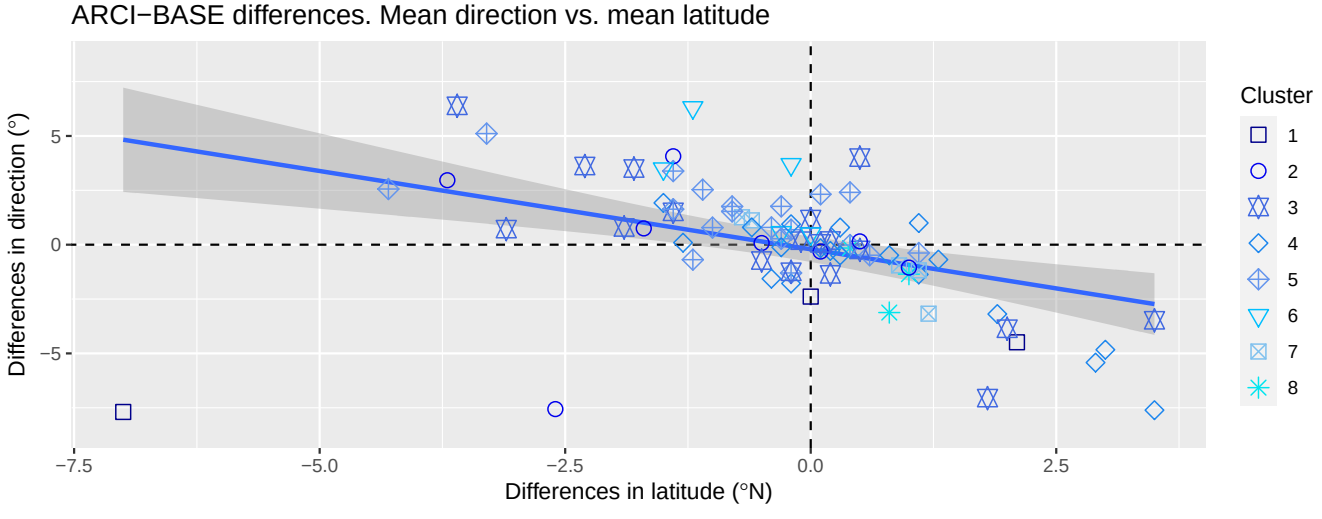

Figure A2. ARCI-BASE differences in mean direction versus ARCI-BASE differences in mean incidence latitude. Each set of shape and colour represents an ARCI cluster. The linear regression model is plotted with a blue line and the grey area represents the 95% confidence level interval.

https://doi.org/10.5194/egusphere-2023-1155
Preprint. Discussion started: 6 July 2023

References

Algarra, I., Nieto, R., Ramos, A. M., Eiras-Barca, J., Trigo, R. M., and Gimeno, L.: Significant increase of global anomalous moisture uptake feeding landfalling Atmospheric Rivers, Nature Communications, 11, 5082, https://doi.org/10.1038/s41467-020-18876-w, 2020.

Brands, S., Gutiérrez, J., and San-Martin, D.: Twentieth-century atmospheric river activity along the west coasts of Europe and North America: algorithm formulation, reanalysis uncertainty and links to atmospheric circulation patterns, Climate Dynamics, 48, 2771–2795, https://doi.org/10.1007/s00382-016-3095-6, 2017.

Chakraborty, S., Guan, B., Waliser, D. E., da Silva, A. M., Uluatam, S., and Hess, P.: Extending the Atmospheric River Concept to Aerosols: Climate and Air Quality Impacts, Geophysical Research Letters, 48, https://doi.org/https://doi.org/10.1029/2020GL091827, 2021.

Eiras-Barca, J., Lorenzo, N., Taboada, J., Robles, A., and Miguez-Macho, G.: On the relationship between atmospheric rivers, weather types and floods in Galicia (NW Spain), Natural Hazards and Earth System Sciences, 18, 1633–1645, https://doi.org/10.5194/nhess-18-1633-2018, 2018.

Eiras-Barca, J., Ramos, A. M., Algarra, I., Vázquez, M., Dominguez, F., Miguez-Macho, G., Nieto, R., Gimeno, L., Taboada, J., and Ralph, F. M.: European West Coast atmospheric rivers: A scale to characterize strength and impacts, Weather and Climate Extremes, 31, 100 305, https://doi.org/https://doi.org/10.1016/j.wace.2021.100305, 2021.

Fast, J. D., Gustafson Jr., W. I., Easter, R. C., Zaveri, R. A., Barnard, J. C., Chapman, E. G., Grell, G. A., and Peckham, S. E.: Evolution of ozone, particulates, and aerosol direct radiative forcing in the vicinity of Houston using a fully coupled meteorology-chemistry-aerosol model, Journal of Geophysical Research: Atmospheres, 111, https://doi.org/https://doi.org/10.1029/2005JD006721, 2006.

Forkel, R., Balzarini, A., Baró, R., Bianconi, R., Curci, G., Jiménez-Guerrero, P., Hirtl, M., Honzak, L., Lorenz, C., Im, U., Pérez, J. L., Pirovano, G., San José, R., Tuccella, P., Werhahn, J., and Žabkar, R.: Analysis of the WRF-Chem contributions to AQMEII phase2 with respect to aerosol radiative feedbacks on meteorology and pollutant distributions, Atmospheric Environment, 115, 630–645, https://doi.org/https://doi.org/10.1016/j.atmosenv.2014.10.056, 2015.

Gimeno, L., Nieto, R., Vázquez, M., and Lavers, D.: Atmospheric rivers: A mini-review, Frontiers in Earth Science, 2, https://doi.org/10.3389/feart.2014.00002, 2014.

Gimeno, L., Algarra, I., Eiras-Barca, J., Ramos, A. M., and Nieto, R.: Atmospheric river, a term encompassing different meteorological patterns, WIREs Water, 8, e1558, https://doi.org/https://doi.org/10.1002/wat2.1558, 2021.

Grell, G. A., Peckham, S. E., Schmitz, R., McKeen, S. A., Frost, G., Skamarock, W. C., and Eder, B.: Fully coupled "online" chemistry within the WRF model, Atmospheric Environment, 39, 6957–6975, https://doi.org/https://doi.org/10.1016/j.atmosenv.2005.04.027, 2005.

Guan, B., Waliser, D. E., Molotch, N. P., Fetzer, E. J., and Neiman, P. J.: Does the Madden–Julian Oscillation Influence Wintertime Atmospheric Rivers and Snowpack in the Sierra Nevada?, Monthly Weather Review, 140, 325 – 342, https://doi.org/10.1175/MWR-D-11-00087.1, 2012.

Jacob, D., Petersen, J., Eggert, B., Alias, A., Christensen, O. B., Bouwer, L. M., Braun, A., Colette, A., Déqué, M., Georgievski, G., Georgopoulou, E., Gobiet, A., Menut, L., Nikulin, G., Haensler, A., Hempelmann, N., Jones, C., Keuler, K., Kovats, S., Kröner, N., Kotlarski, S., Kriegsmann, A., Martin, E., van Meijgaard, E., Moseley, C., Pfeifer, S., Preuschmann, S., Radermacher, C., Radtke, K., Rechid, D., Rounsevell, M., Samuelsson, P., Somot, S., Soussana, J.-F., Teichmann, C., Valentini, R., Vautard, R., Weber, B., and Yiou, P.: EURO-CORDEX: new high-resolution climate change projections for European impact research, Regional Environmental Change, 14, 563–578, https://doi.org/10.1007/s10113-013-0499-2, 2014.

https://doi.org/10.5194/egusphere-2023-1155
Preprint. Discussion started: 6 July 2023

Jerez, S., Palacios-Peña, L., Gutiérrez, C., Jiménez-Guerrero, P., López-Romero, J. M., Pravia-Sarabia, E., and Montávez, J. P.: Sensitivity of surface solar radiation to aerosol–radiation and aerosol–cloud interactions over Europe in WRFv3.6.1 climatic runs with fully interactive aerosols, Geoscientific Model Development, 14, 1533–1551, https://doi.org/10.5194/gmd-14-1533-2021, 2021.

Lavers, D. A., Villarini, G., Allan, R. P., Wood, E. F., and Wade, A. J.: The detection of atmospheric rivers in atmospheric reanalyses and their links to British winter floods and the large-scale climatic circulation, Journal of Geophysical Research: Atmospheres, 117, https://doi.org/https://doi.org/10.1029/2012JD018027, 2012.

Lin, Y.-L., Farley, R. D., and Orville, H. D.: Bulk Parameterization of the Snow Field in a Cloud Model, Journal of Climate and Applied Meteorology, 22, 1065–1092, http://www.jstor.org/stable/26180993, 1983.

López-Romero, J. M., Montávez, J. P., Jerez, S., Lorente-Plazas, R., Palacios-Peña, L., and Jiménez-Guerrero, P.: Precipitation response to aerosol–radiation and aerosol–cloud interactions in regional climate simulations over Europe, Atmospheric Chemistry and Physics, 21, 415–430, https://doi.org/10.5194/acp-21-415-2021, 2021.

Lorente-Plazas, R., Mitchell, T. P., Mauger, G., and Salathé, E. P.: Local Enhancement of Extreme Precipitation during Atmospheric Rivers as Simulated in a Regional Climate Model, Journal of Hydrometeorology, 19, 1429 – 1446, https://doi.org/10.1175/JHM-D-17-0246.1, 2018.

Lorente-Plazas, R., Montavez, J. P., Ramos, A. M., Jerez, S., Trigo, R. M., and Jimenez-Guerrero, P.: Unusual Atmospheric-River-Like Structures Coming From Africa Induce Extreme Precipitation Over the Western Mediterranean Sea, Journal of Geophysical Research: Atmospheres, 125, https://doi.org/https://doi.org/10.1029/2019JD031280, 2020.

O'Brien, T. A., Payne, A. E., Shields, C. A., Rutz, J., Brands, S., Castellano, C., Chen, J., Cleveland, W., DeFlorio, M. J., Goldenson, N., Gorodetskaya, I. V., Díaz, H. I., Kashinath, K., Kawzenuk, B., Kim, S., Krinitskiy, M., Lora, J. M., McClenny, B., Michaelis, A., O'Brien, J. P., Patricola, C. M., Ramos, A. M., Shearer, E. J., Tung, W.-W., Ullrich, P. A., Wehner, M. F., Yang, K., Zhang, R., Zhang, Z., and Zhou, Y.: Detection Uncertainty Matters for Understanding Atmospheric Rivers, Bulletin of the American Meteorological Society, 101, E790 – E796, https://doi.org/https://doi.org/10.1175/BAMS-D-19-0348.1, 2020.

Palacios-Peña, L., Baró, R., Baklanov, A., Balzarini, A., Brunner, D., Forkel, R., Hirtl, M., Honzak, L., López-Romero, J. M., Montávez, J. P., Pérez, J. L., Pirovano, G., San José, R., Schröder, W., Werhahn, J., Wolke, R., Žabkar, R., and Jiménez-Guerrero, P.: An assessment of aerosol optical properties from remote-sensing observations and regional chemistry–climate coupled models over Europe, Atmospheric Chemistry and Physics, 18, 5021–5043, https://doi.org/10.5194/acp-18-5021-2018, 2018.

Palacios-Peña, L., Jiménez-Guerrero, P., Baró, R., Balzarini, A., Bianconi, R., Curci, G., Landi, T. C., Pirovano, G., Prank, M., Riccio, A., Tuccella, P., and Galmarini, S.: Aerosol optical properties over Europe: an evaluation of the AQMEII Phase 3 simulations against satellite observations, Atmospheric Chemistry and Physics, 19, 2965–2990, https://doi.org/10.5194/acp-19-2965-2019, 2019.

Palacios-Peña, L., Montávez, J. P., López-Romero, J. M., Jerez, S., Gómez-Navarro, J. J., Lorente-Plazas, R., Ruiz, J., and Jiménez-Guerrero, P.: Added Value of Aerosol-Cloud Interactions for Representing Aerosol Optical Depth in an Online Coupled Climate-Chemistry Model over Europe, Atmosphere, 11, https://doi.org/10.3390/atmos11040360, 2020.

Payne, A. E., Demory, M.-E., Leung, L. R., Ramos, A. M., Shields, C. A., Rutz, J. J., Siler, N., Villarini, G., Hall, A., and Ralph, F. M.: Responses and impacts of atmospheric rivers to climate change, Nature Reviews Earth & Environment, 1, 143–157, https://doi.org/10.1038/s43017-020-0030-5, 2020.

Pravia-Sarabia, E., Halifa-Marín, A., Gómez-Navarro, J. J., Palacios-Peña, L., Jiménez-Guerrero, P., and Montávez, J. P.: On the role of aerosols in the production of orographically-induced extreme rainfall in near-maritime environments, Atmospheric Research, 268, 106 001, https://doi.org/https://doi.org/10.1016/j.atmosres.2021.106001, 2022.

https://doi.org/10.5194/egusphere-2023-1155
Preprint. Discussion started: 6 July 2023

Ralph, F. M., Neiman, P. J., and Wick, G. A.: Satellite and CALJET Aircraft Observations of Atmospheric Rivers over the Eastern North Pacific Ocean during the Winter of 1997/98, Monthly Weather Review, 132, 1721–1745, https://doi.org/10.1175/1520-0493(2004)132<1721:SACAOO>2.0.CO;2, 2004.

Ralph, F. M., Neiman, P. J., Kiladis, G. N., Weickmann, K., and Reynolds, D. W.: A Multiscale Observational Case Study of a Pacific Atmospheric River Exhibiting Tropical—Extratropical Connections and a Mesoscale Frontal Wave, Monthly Weather Review, 139, 1169 – 1189, https://doi.org/10.1175/2010MWR3596.1, 2011.

Ralph, F. M., Rutz, J. J., Cordeira, J. M., Dettinger, M., Anderson, M., Reynolds, D., Schick, L. J., and Smallcomb, C.: A Scale to Characterize the Strength and Impacts of Atmospheric Rivers, Bulletin of the American Meteorological Society, 100, 269 – 289, https://doi.org/https://doi.org/10.1175/BAMS-D-18-0023.1, 2019.

Raluy-López, E., Montávez, J. P., and Jiménez-Guerrero, P.: AIRA (Atmospheric Rivers Identification Algorithm) input dataset and results, https://doi.org/10.5281/zenodo.7898400, 2023a.

Raluy-López, E., Montávez, J. P., and Jiménez-Guerrero, P.: AIRA (Atmospheric Rivers Identification Algorithm) software, https://doi.org/10.5281/zenodo.7885383, 2023b.

Skamarock, W. C., Klemp, J. B., Dudhia, J., Gill, D. O., Barker, D., Duda, M. G., and Powers, J. G.: A Description of the Advanced Research WRF Version 3, University Corporation for Atmospheric Research, (No. NCAR/TN-475+STR), https://doi.org/10.5065/D68S4MVH, 2008.

Trigo, R., Ramos, C., Pereira, S., Ramos, A., Zêzere, J., and Liberato, M.: The deadliest storm of the 20th Century striking Portugal: Flood impacts and atmospheric circulation, Journal of Hydrology, 541, https://doi.org/10.1016/j.jhydrol.2015.10.036, 2015.

Zhang, P., Chen, G., Ting, M., Ruby Leung, L., Guan, B., and Li, L.: More frequent atmospheric rivers slow the seasonal recovery of Arctic sea ice, Nature Climate Change, 13, 266–273, https://doi.org/10.1038/s41558-023-01599-3, 2023.

Zhu, Y. and Newell, R. E.: A Proposed Algorithm for Moisture Fluxes from Atmospheric Rivers, Monthly Weather Review, 126, 725–735, https://doi.org/10.1175/1520-0493(1998)126<0725:APAFMF>2.0.CO;2, 1998.